J Geod (2011) 85:585–596
DOI 10.1007/s00190-011-0461-3

ORIGINAL ARTICLE

Alternative method for angular rate determination within the GOCE gradiometer processing

C. Stummer · T. Fecher · R. Pail

Received: 14 September 2010 / Accepted: 11 March 2011 / Published online: 29 March 2011

Abstract The most crucial part of the GOCE gradiometer processing is, besides the internal calibration of the gradiometer, the determination of the satellite's inertial angular rate. This paper describes a new method for the angular rate determination. It is based on the stochastic properties of the GOCE star sensors and the gradiometer. The attitude information of both instrument types is combined at the level of angular rates. The combination is done in the spectral domain by Wiener filtering, and thus using an optimal relative weighting of the star sensor and gradiometer attitude information. Since the complete processing chain from raw measurements to gravity field solutions is performed, the results are not only analyzed at the level of gravity gradients, but also of gravity field solutions. Compared to the nominal method, already the resulting gravity gradients show a significantly improved performance for the frequencies (mainly) below the gradiometer measurement bandwidth. This can be verified by analysis of the gravity gradient trace. The improvement is propagated to the level of gravity field models, where a better accuracy can be observed for selected groups of coefficients at characteristic bands at orders $k \times 16$, with integer k, up to high harmonic degrees.

Keywords GOCE · Gradiometer · Star sensor · Accelerations · Angular rate · Gravity gradients

C. Stummer (✉) · T. Fecher · R. Pail
Institut für Astronomische und Physikalische Geodäsie (IAPG),
Technische Universität München, Arcisstr. 21,
80290 Munich, Germany
e-mail: stummer@bv.tum.de

1 Introduction

The gravity field and steady-state ocean circulation explorer (GOCE) mission was launched successfully on 17 March 2009. Since the beginning of the mission operational phase in September 2009, it is gathering data of the Earth's gravity field with unprecedented precision. GOCE is the first core explorer mission in the Living Planet programme of the European Space Agency (ESA). The GOCE mission objective is to model the Earth's static gravity field with an accuracy of 2 cm in geoid, and 1 mGal in gravity anomalies, at a spatial resolution of 100 km (Drinkwater et al. 2007).

The core instrument of GOCE is an electrostatic gravity gradiometer (EGG), which consists of six accelerometers mounted on three mutually orthogonal axes. Moreover, the satellite is equipped with a GPS instrument for high-low satellite-to-satellite tracking (SST), and three star sensors (STR) to determine the absolute orientation in space.

The EGG measurements are used to derive common mode (CM) and differential mode (DM) accelerations. CM accelerations represent the sum of all non-conservative (non-gravitational) forces acting on the satellite, and are input signal of the drag-free control (DFC) system. It keeps the satellite in free fall at constant altitude using ion-thrusters as actuators. From the DM accelerations, finally the satellite gravity gradients (GG) are derived (Cesare and Catastini 2008), which represent the key product to model the Earth's gravity field. One important aspect of the high performance of the GOCE mission is the fact that the EGG is not only the key driver to measure CM and DM linear accelerations, but also rotational accelerations, which are combined with the STR observations. After this angular rate reconstruction (ARR), GG at the one hand, and the attitude information of the satellite at the other hand, are derived.

The GOCE data processing at ground level is performed at several levels (Drinkwater et al. 2007). While the processing of raw instrument time series to calibrated products (Level 0 to Level 1b) is deduced from ESA's Payload Data Segment (PDS; Frommknecht et al. 2010), the scientific data processing (Level 1b to Level 2), i.e. the processing of precise orbits and GOCE gravity fields, is performed by the high-level processing facility (HPF; Rummel et al. 2004). First, GOCE gravity field models based on 71 days of GOCE data, using three complementary processing strategies, are already publicly available (Bruinsma et al. 2010; Pail et al. 2010; Migliaccio et al. 2010).

One of the key tasks of the Level 1b (L1b) processing is the internal calibration of the GOCE gradiometer, i.e., the derivation of the so-called inverse calibration matrices (ICMs; Cesare and Catastini 2008) reflecting the very small imperfections of the gradiometer assembly such as scale factors, misalignments of the individual accelerometers, and non-orthogonalities of the axes. In addition to the standard method implemented in the PDS (Cesare and Catastini 2008), several alternative methods have been investigated (e.g., Kern et al. 2007), also using star tracker data (Visser 2008; Rispens and Bouman 2009).

Another main task of the L1b processing is the ARR. In this paper, a method for the common treatment of star tracker and gradiometer observations for the purpose of ARR is proposed, which is an alternative to the standard processing of the PDS (Cesare et al. 2008). This newly proposed method is based on a Wiener filter approach (Papoulis 1984) for combination. In addition to the derivation of L1b gradient and attitude information, also the improvement in the frame of the (Level 2) gravity field processing when using these newly derived products is investigated. Thus, the complete chain from initial instrument time series to gravity field models is covered.

In Sect. 2, the methodology is presented, with special emphasis on the new Wiener filter method. Since the definition of the Wiener filter is based on the stochastic models for STR and EGG, they are reviewed in Sect. 3. In Sect. 4, the numerical aspects of the implemented improvements within the GOCE gradiometer processing chain are discussed. Section 5 focuses on the results of the improved gradiometer processing and their impact on gravity field solutions. Section 6 contains conclusions and outlook.

2 Methodology

In this section, the methodology is described, starting with a brief description of the EGG L1b processing chain. Moreover, the data sets used for the computations in this paper are addressed. Besides a short description of the nominal method for ARR, the methodology for the new ARR method is presented.

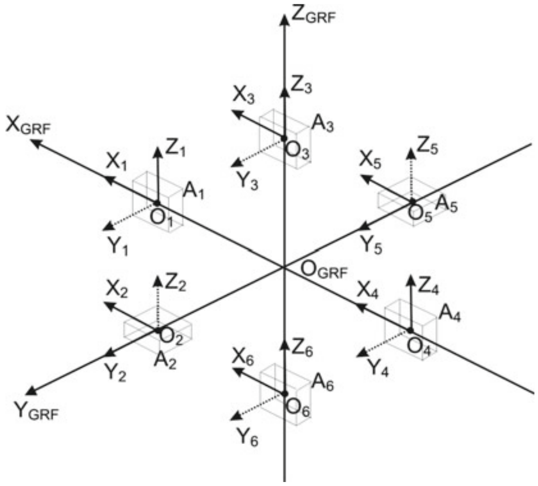

Fig. 1 Arrangement of the six accelerometers ($A1$–$A6$) of the GOCE gradiometer within the GRF. The ultra-sensitive accelerometer axes are shown by *solid arrows*. The *dashed arrows* indicate the less sensitive accelerometer axes

2.1 GOCE gradiometer processing chain

The GOCE EGG L1b processing chain (Cesare et al. 2008; Stummer and Rispens 2009) starts with the measured control voltages (8 per accelerometer), which are proportional to the accelerations acting on the proof mass of an accelerometer (Johannessen 1999). The control voltages are transformed into three linear accelerations per accelerometer, which are rotated into a common reference frame, the gradiometer reference frame (GRF, Gruber et al. 2010b). The arrangement of the six accelerometers within the GOCE gradiometer is displayed in Fig. 1.

The measured accelerations **a** do not only contain the GG, but consist basically of four terms (Rispens and Bouman 2009)

$$\mathbf{a} = -\mathbf{V} \cdot \mathbf{r} + \boldsymbol{\omega} \times (\boldsymbol{\omega} \times \mathbf{r}) + \dot{\boldsymbol{\omega}} \times \mathbf{r} + \mathbf{D}, \tag{1}$$

with **r** the distance between the accelerometer and the satellite's center of mass (Rummel 1986). Beside the GG tensor (**V**), which is composed of the second order derivatives of the gravitational potential, there are measured inertial accelerations, such as the centrifugal accelerations due to the rotation of the satellite in space (term with angular rate $\boldsymbol{\omega}$), and the Euler term due to the satellite's angular accelerations ($\dot{\boldsymbol{\omega}}$). Moreover, also residual non-conservative accelerations (**D**), like not perfectly compensated air drag and solar radiation pressure, are sensed. The linear accelerations can be deduced from the mean of two accelerations in the same direction, the CM accelerations

$$a_{c,k,l,i} = \frac{1}{2}\left(a_{k,i} + a_{l,i}\right), \tag{2}$$

with k,l the number of the accelerometer and i the measurement direction. Theoretically, the CM accelerations do not affect the GG measurement, since the GG are determined from the DM accelerations

$$a_{d,k,l,i} = \frac{1}{2}\left(a_{k,i} - a_{l,i}\right). \tag{3}$$

This is the principle of common mode rejection. In reality, a small part of the CM accelerations is leaking into the measured DM due to the fact that there are some small gradiometer imperfections, like scale factors errors of the accelerometers or rotational misalignments of the accelerometers. Therefore, the gradiometer imperfections have to be taken into account in the nominal L1b processing by application of the ICMs (Rispens and Bouman 2009). After this correction, only rotational signal remains in the DM to be taken into account when forming the GG. This signal still includes, apart from the GG, the accelerations due to the centrifugal force acting on the satellite. Therefore, the centrifugal part has to be subtracted from the DM accelerations, according to the equations:

$$V_{xx} = -\frac{2a_{d,1,4,x}}{L_x} - \omega_y^2 - \omega_z^2 \tag{4}$$

$$V_{yy} = -\frac{2a_{d,2,5,y}}{L_y} - \omega_x^2 - \omega_z^2 \tag{5}$$

$$V_{zz} = -\frac{2a_{d,3,6,z}}{L_z} - \omega_x^2 - \omega_y^2 \tag{6}$$

with $L_{x/y/z}$ the distance between the two accelerometers in direction x, y or z. For this purpose, the angular velocity of the spacecraft has to be known very accurately over the entire frequency range. For GOCE, there are two complementary kinds of instruments available to deliver precise attitude information. On the one hand, there are the STR which measure very accurately the absolute orientation of the satellite in space, but which are less accurate for high frequencies. On the other hand, there is the gradiometer itself, which is able to measure with its transversal components the angular accelerations experienced by the satellite:

$$\dot{\omega}_x = -\frac{a_{d,3,6,y}}{L_z} + \frac{a_{d,2,5,z}}{L_y} \tag{7}$$

$$\dot{\omega}_y = -\frac{a_{d,1,4,z}}{L_x} + \frac{a_{d,3,6,x}}{L_z} \tag{8}$$

$$\dot{\omega}_z = -\frac{a_{d,2,5,x}}{L_y} + \frac{a_{d,1,4,y}}{L_x} \tag{9}$$

The highest accuracy of the gradiometer measurements is expected to be achieved in the so-called measurement bandwidth (MBW) from 5–100 mHz. Below, the accelerometer measurements are expected to suffer from a $1/f$-increase of noise at the low frequencies. These are the accelerometer properties which are given by instrument design. In Sect. 3.2, an attempt is made to verify these properties with real data. To find the best angular rate estimation over the entire frequency range, a combination between the two sets of attitude information, one coming from STR and one coming from EGG, has to be done. In the nominal processing chain this combination, or ARR, is done in the time domain by means of Kalman filtering. The purpose of the present work is to propose a new method for angular rate determination based on the optimal combination of STR and EGG derived angular rates by means of Wiener filtering in the frequency domain.

2.2 Data

All computations presented in this paper are based on 26 days of GOCE data (01/11/2009 to 26/11/2009), available via ESA's data portal EOLI-SA. The generation of the GG is carried out, starting from the gradiometer control voltages, which are contained in the *EGG_NOM_1b* files. The results have been checked for consistency with the nominal data. For the angular rate determination also the STR data (in *STR_QUA* and *STR_QUB* files) are needed. Additional parameters for the gradiometer processing have been taken from the EGG auxiliary database (*AUX_EGG_DB*). Moreover, the ICMs from the third dedicated satellite shaking, computed by the so-called *ESA-L* method (Lamarre 2008; Kern et al. 2007, in file *AUX_ICM_2C*;) have been applied continuously throughout all computations.

2.3 Nominal angular rate reconstruction

The nominal ARR (Cesare and Catastini 2008) does the combination of STR and EGG data by means of Kalman filtering in the time domain. The main inputs are the EGG angular accelerations and the STR quaternions. In principle, the method consists of a prediction and a correction step. Within the prediction step, the angular rates (derived from integration of the gradiometer angular accelerations) are used to rotate the attitude quaternions from the actual epoch to the next. Thus, for the subsequent epoch, besides the measured STR quaternion, also a predicted attitude quaternion is available. In the frame of the correction step of the Kalman filter, the correction for the current attitude quaternion and the angular rate estimates is computed from the difference between these two sets of quaternions. The gains of the estimator are derived from pre-launch measurement performance models of the gradiometer and the STR.

In Sect. 3.1, it will be shown that the actual instrument performance (mainly of STR) is not perfectly in agreement with pre-launch expectations. The output of the ARR is the inertial angular rates of the gradiometer about the axes of the GRF, and the inertial attitude quaternions (IAQ), defining the attitude of the GRF in the inertial reference frame (IRF).

2.4 Wiener method for angular rate determination

The newly developed method for angular rate determination performs a spectral combination of the three angular rate components (of STR and EGG) about the axes of the GRF in the IRF. To obtain angular rates from the STR quaternions, first a rotation from the star sensor reference frame (SSRF, Gruber et al. 2010a) into the GRF has to be carried out. This can be done using the known rotation matrices from SSRF to GRF (in file AUX_EGG_DB). Further on, the STR angular rates are obtained from the rotated quaternions by employing the Poisson's equations (Wittenburg 1977; Cesare et al. 2008). To obtain angular rates from the gradiometer, the EGG angular accelerations from Eqs. 7–9 are numerically integrated in the frequency domain (Best 1991). The EGG angular rates are already in the desired reference frame, the GRF. The optimal combination between STR and EGG angular rate is performed by weighting the angular rate components according to their noise power spectral densities (PSD). The weights h_k for the Wiener filter (Papoulis 1984) are obtained according to

$$h\,(\mathrm{STR})_k = \frac{\sigma_k^2\,(\mathrm{EGG})}{\sigma_k^2\,(\mathrm{EGG}) + \sigma_k^2\,(\mathrm{STR})} \tag{10}$$

$$h\,(\mathrm{EGG})_k = \frac{\sigma_k^2\,(\mathrm{STR})}{\sigma_k^2\,(\mathrm{EGG}) + \sigma_k^2\,(\mathrm{STR})} \tag{11}$$

with σ_k^2 being the variances of the gradiometer (EGG) and star sensor (STR) noise at frequency k, respectively. Therefore, the sum of the weights equals one for all frequencies

$$h\,(\mathrm{STR})_k + h\,(\mathrm{EGG})_k = 1. \tag{12}$$

The merging of the angular rates is performed componentwise according to

$$\begin{aligned} F\,(\mathrm{merge})_k &= F\,(\mathrm{STR})_k \cdot h\,(\mathrm{STR})_k \\ &\quad + F\,(\mathrm{EGG})_k \cdot h\,(\mathrm{EGG})_k \end{aligned} \tag{13}$$

with F being the frequency domain representation of the EGG, STR or merged (merge) angular rate components at frequency k. The merged angular rates in the frequency domain are transformed back into the time domain to obtain the sought after combined angular rates.

Since the weights of the Wiener filter are based on the noise characteristics of the star sensor and gradiometer measurements, representative noise power spectral densities, for both, STR and EGG angular rates have to be derived, as shown in the following section.

3 Stochastic models

The exact separation of signal from noise in the measurements of EGG and STR is not possible. Therefore, only assumptions about their noise characteristics can be made. Nevertheless, from the GOCE data themselves some lucid indicators can be derived how to describe and model the noise of the STR and the EGG.

3.1 Star sensors

Currently, in the nominal GOCE processing only one star sensor is used as input for the ARR. Actually, GOCE contains a set of three STR and nominally, the data from two of them are available. We will, therefore, investigate the benefit of combining the two available STR. Its effect on the nominal ARR as well as the impact on the Wiener method will be highlighted at the level of GG, and also at the level of a gravity field solution based on these GG.

The accuracy of each GOCE STR can be characterized by the pointing accuracy of the coordinate axes of the respective SSRF, with the z-axis being aligned with the boresight direction, and the x- and y-axes lying in the CCD plain of the STR (Frommknecht 2008). Due to the geometry between the direction to the observed stars and the coordinate axes of the SSRF, it is possible to determine the boresight axis of the STR more accurate than the other two axes. For the GOCE STR the relative accuracy (RA) in-flight is given with 10 μ rad or 2 arcseconds for the ultra sensitive (US) boresight axis, and with 100 μ rad or 20 arcseconds for the orientation of the other two less sensitive (LS) axes (Jørgensen 2003). For the accuracy of a rotation about the SSRF axes, this consequently means that the rotation about the boresight is worse than the rotations about the other two STR axes. The corresponding error spectrum of the orientation measurements is regarded as white noise.

When the attitude measurements of the individual STR are transformed from SSRF to GRF, the measurements of the LS axes leak into the US components. In Fig. 2, this effect is shown by the PSD of the angular rate of STR 2 in the GRF. For frequencies above approximately 10 mHz, the STR noise is dominating the signal and shows an f-increase. This results from the differentiation process (cf. Sect. 2.4) of white noise at quaternion level. Moreover, one observes that for STR 2 the angular rate component about the x-axis in GRF (blue curve) is smaller than the other two components. This is due to the beneficial geometry of STR 2 with respect to the GRF in this case, with the boresight axis of STR 2 being perpendicular to the x-axis in GRF. Thus, the rotation about the x-axis (GRF) is determined by US measurements only. In the other two angular rate components, the impact of the LS STR axes is increasing the noise level. Note that the Fig. 2 shall only serve as an example for a PSD of the angular rate in GRF, here from STR 2. The respective PSD derived from STR 1 or STR 3 (not shown) look different, according to their arrangement with respect to GRF.

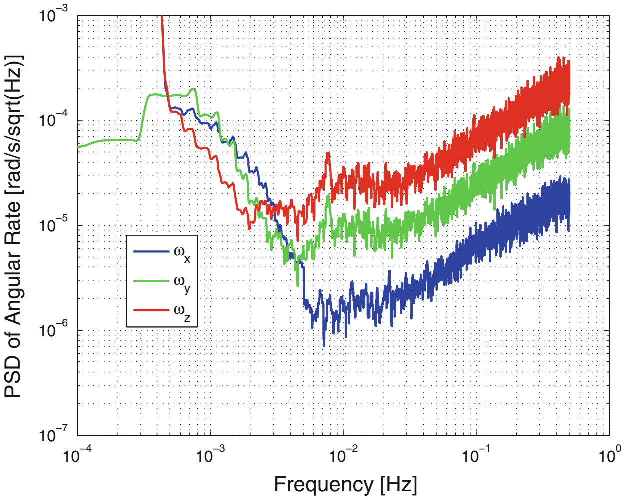

Fig. 2 PSD of angular rate of STR 2 in the GRF

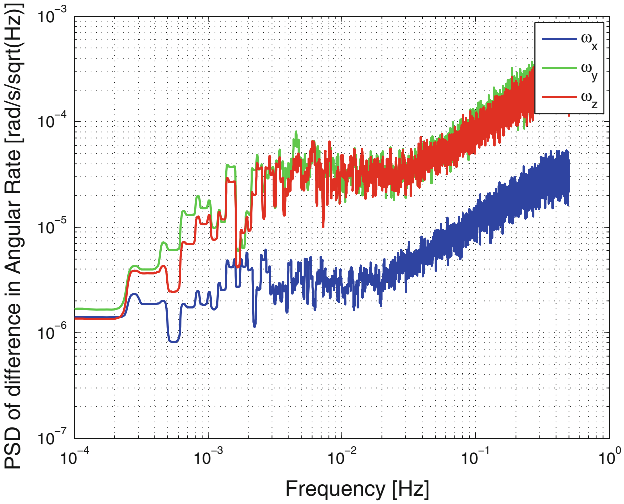

Fig. 3 PSD of difference in angular rate (in GRF) of STR 1 and STR 2

From what was shown so far, the STR (and their noise with its f-increase) seem to behave according to expectations from pre-launch. Another strategy to get an impression on the actual STR noise is to transform the quaternions of the two available STR from their specific SSRF into GRF, to derive the two corresponding sets of angular rates, and to analyze the differences between them.

Figure 3 shows the PSD of the differences in the angular rates exemplarily of STR 1 and STR 2. It can be noted that at very high frequencies from about 50 mHz, and beyond the actual STR noise seems to behave as expected with an f-increase. In comparison to Fig. 2, we observe a strongly increased noise level for the y-component (green), which can be attributed to the influence of STR 1 in this case. (For the angular rate y-component, the geometry of STR 1 with respect to GRF is disadvantageous compared to the one of STR 2.) For frequencies lower than about 50 mHz the actual STR noise does not continue with the f-behavior, as expected from simulation, but it is approximately flat. The reason is that the STR noise shows at attitude level a significant repeat pattern at the frequency of one cycle per revolution (1 cpr $\approx 1.85 \times 10^{-4}$ Hz) and with a $1/f$-decreasing magnitude towards higher frequencies also at the corresponding harmonics k cpr, with integer k. This $1/f$-behavior at quaternion level is propagated to a flat noise spectrum at angular rate level, due to the underlying differentiation process.

In summary, it is shown with real data that the three angular rate components in GRF derived from the individual star sensors have different accuracies, due to coupling of the LS STR axes into the US ones, as expected. On top of that, the STR data have a (much) higher noise compared to expectations for the frequencies of 1 cpr and the corresponding harmonics. This higher noise in the STR data has a strong effect on the determination of the best cross-over frequency between STR and EGG within the new ARR method (see Sect. 4.3).

3.2 Gradiometer

The GOCE EGG consists of six three-axis accelerometers, each of them having two US axes and one, which is LS by a factor of about 100. To check the EGG performance, one can form the differences between the CM accelerations in one direction, e.g., in x-direction of GRF, see Fig. 4.With the three sets of CM accelerations the (same) linear accelerations acting on the satellite are measured. Since all six accelerometers are mounted in such a way that the x-direction of GRF is measured by US axes only (cf. Fig. 1), also the three combinations of CM accelerations in Fig. 4 only contain US measurements. From simple error propagation, one can derive $\sigma_{a\_comb} = \sqrt{2}\sigma_{a\_c/d\_US}$, with σ_{a_comb} the standard deviation of the CM combination, and σ_{a_c/d_US} the standard deviation of the corresponding CM or DM acceleration. Moreover, $\sigma_{a\_c/d\_US} = \left(1/\sqrt{2}\right)\sigma_{a\_US}$, with σ_{a_US} the standard deviation of an individual US acceleration measurement. Thus, $\sigma_{a\_comb} \approx \sigma_{a\_US}$ holds, and the three curves in Fig. 4 can be taken as a good indicator of the real US acceleration noise (about $10^{-11}\mathrm{m/s}^2/\sqrt{\mathrm{Hz}}$ in the MBW). The exact noise level within the MBW shall not be further discussed here, since it is not relevant for the performance of the Wiener filter, see Sect. 4.3. It shall only be highlighted that also in the EGG data there are peaks in the noise PSD at the frequency corresponding to 1 cpr and, with a decreasing magnitude, also at the corresponding harmonics. Moreover, it indicates an EGG acceleration low frequency behaviour of about $1/f$ below the MBW. To derive angular rates from the EGG, the angular accelerations (Eqs. 7–9) have to be integrated, as described in Sect. 2.4. The effect of integration on the error spectrum is a damping of the higher frequencies.

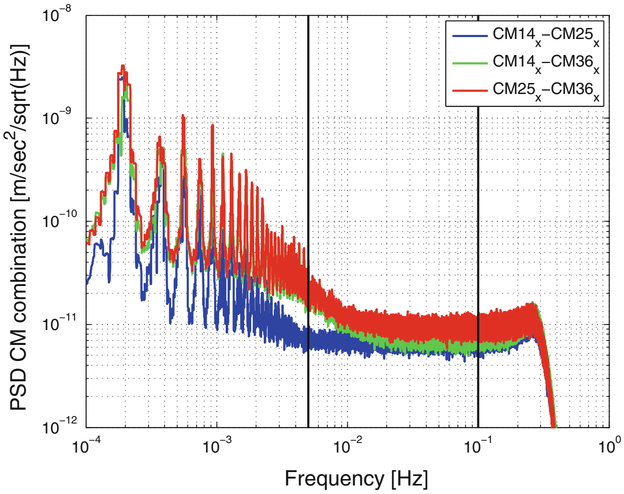

Fig. 4 PSD of the differences in common-mode accelerations in GRF, *x*-direction

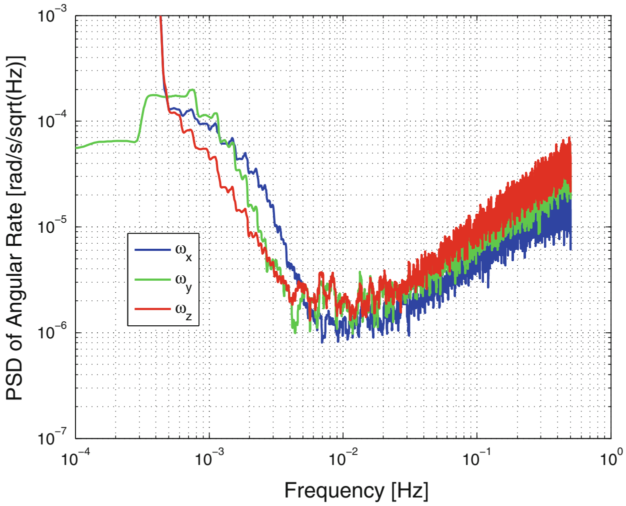

Fig. 5 PSD of angular rate (in GRF) from STR combination

The $1/f$-increase at acceleration level below the MBW is, therefore, propagated to a $1/f^2$-increase at angular rate level. These are the main drivers of the noise characteristics of the EGG in the frame of the Wiener method for ARR (see Sect. 4.3).

4 Alternative processing strategies

In this section, the implemented processing strategies for gradiometer and star sensor data are presented. Besides the new method for ARR itself, also a combination of the available STR data and a new method for the computation of the IAQ are discussed.

4.1 Star sensor combination

Since for GOCE the data from two STR are available simultaneously, it is possible to combine these two sets of quaternions in such a way that only the US measurements are used. To be more precise, only the boresight (or z-axis of SSRF) of the two available STR is used, and a new frame is created with the new SSRF x-axis pointing to z1+z2, the new y-axis pointing to z1−z2 and the new z-axis pointing to the cross-product of the new x- and y-axes. Figure 5 shows the angular rates derived from a STR combination (here STR 1 and STR 2). Due to the STR combination, it is possible to decrease the noise of the two inferior angular rate components in GRF (compare to Fig. 2) to approximately the noise of the very accurate component. In Sect. 5, the impact of applying the STR combination on the nominal and the new method for ARR is discussed.

4.2 IAQ calculation

For gravity field computation, not only the GG, but also the attitude of the GRF with respect to the IRF has to be known. Therefore, in the nominal L1b processing, the corresponding IAQ are computed simultaneously with the angular rates about GRF within the ARR. In contrast, the Wiener method for ARR does only provide angular rates but no attitude quaternions. Therefore, also a new strategy for the determination of the IAQ has been developed, with the goal to provide better or similar results than the official IAQ. First, the attitude quaternions from the two available STR are combined, as described in Sect. 4.1. Second, the combined quaternions are low-pass filtered in the frequency domain with a cut-off frequency of 5 mHz. This cut-off frequency is used, because for frequencies higher than that the STR noise is dominating the quaternion signal by far. Therefore, the smoothing of the (combined) quaternions by eliminating the high frequencies (>5 mHz) improves their accuracy. No combination with the gradiometer attitude data is done. In Sect. 5.2, it will be demonstrated that using the new IAQ the accuracy at gravity field level is not significantly affected. Thus, it can be concluded that for the orientation of the GG within the gravity field computation the long wavelength part of the attitude data is essential (Pail 2005).

4.3 Angular rate determination

Based on the findings of Sect. 3, four different sets of STR and EGG noise models have been empirically designed. The four versions of assumed noise have been used within the Wiener method for angular rate determination, each time using the combined STR data. For version 1 (V1), different noise spectral densities for the three angular rate components

Table 1 Version 1 of assumed gradiometer and star sensor angular rate noise

EGG	Below MBW	Within MBW	Above MBW
x/z	$1/f^2$-behavior	10^{-8}	f^2-behavior
y	$1/f^2$-behavior	10^{-9}	f^2-behavior
STR	Below 3 mHz	From 3 to 30 mHz	Above 30 mHz
x	f-behavior	4×10^{-6}	f-behavior
y/z	f-behavior	4×10^{-5}	f-behavior

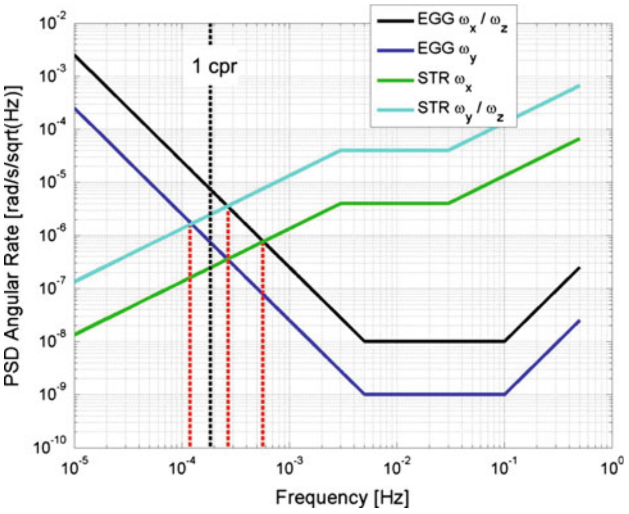

Fig. 6 PSD of assumed STR and EGG angular rate noise: version 1

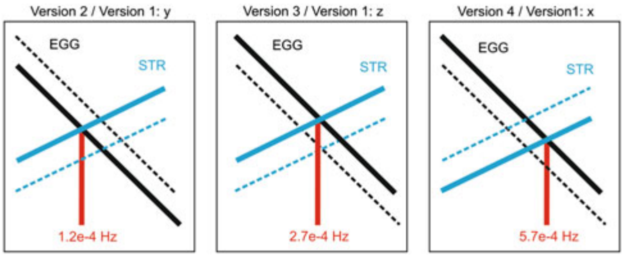

Fig. 7 PSD of assumed STR and EGG angular rate noise: versions 2–4

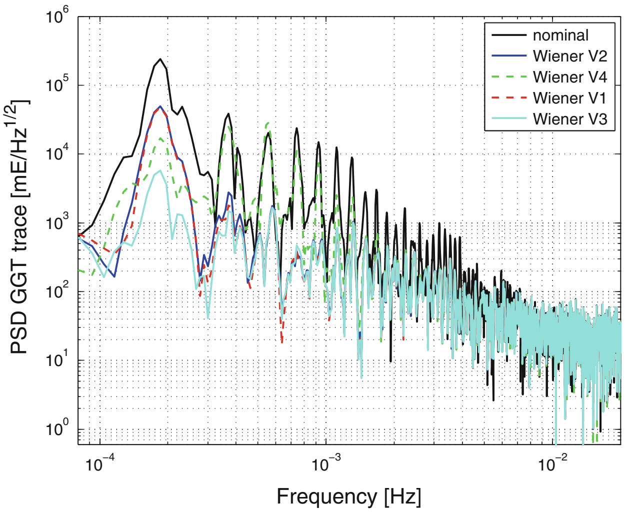

Fig. 8 PSD of GGT trace: impact of different cross-over frequencies between STR and EGG

from STR and from EGG are assumed, according to Table 1 and as illustrated in Fig. 6.

The corresponding cross-over frequencies between STR and EGG are at about 1.2×10^{-4} Hz for the y-component and at about 2.7×10^{-4} and 5.7×10^{-4} Hz for the z- and x-components, respectively (red dashed lines in Fig. 6). For comparison, the 1 cpr frequency is about 1.85×10^{-4} Hz (black dashed line). For versions 2–4 (V2, V3, V4) always the same noise for all three angular rate components has been assumed (for V2 the noise of V1 in y-direction, for V3 the noise of V1 in z-direction, and for V4 the noise of V1 in x-direction), see Fig. 7.

With these four versions of assumed noise the angular rate determination, applying the Wiener method, and using combined STR, has been carried out. The new angular rates have been used to compute four sets of GG (cf. Eqs. 4–6). The quality of the new gradients can be evaluated by comparing the gravity gradient tensor (GGT) trace. From the theory, we know that the Laplace condition holds, i.e., the sum of the three main diagonal GGT components should be zero. In reality, the remaining content in the GGT trace reflects the instrument noise. In our case, this is the noise after the spectral combination of STR and EGG. Since in the spectral combination the STR is mainly used for the low frequencies and the EGG for the medium to high frequencies, we can conclude that also the noise, reflected in the GGT trace, can either be mainly attributed to the STR or to the EGG for the respective frequency bands. Figure 8 shows the GGT trace for all four versions of noise assumptions. Additionally, the trace from the official/nominal L1b gradients (black curve) is given for comparison.

It can be noticed:

- The trace from the nominal gradients (black) has the highest noise content in the frequency range from about 1×10^{-4} to 7×10^{-4} Hz. So, the Wiener method generally gives improved gradients for all four tested versions at the lower end of the MBW and below.
- For the higher frequencies (from about 7×10^{-3} Hz and higher) no improvement with respect to the nominal method can be achieved (see also Sect. 5.1).
- V3 (cyan curve) performs best. The cross-over frequency is in this case at 2.7×10^{-4} Hz, which corresponds to the first minimum (in between the 1 cpr peak and its first harmonic of 2 cpr) in the instrument noise PSD.

- V1 has three different cross-over frequencies for the three angular rate components, and therefore fits best to the expected noise from simulations. However, in this case the GGT trace (red curve) increases significantly at the 1 cpr peak and slightly also at 2 cpr ($\approx 3.7 \times 10^{-4}$ Hz) compared to V3 (cyan).
- In V2, the cross-over frequency for all three components is at 1.2×10^{-4} Hz, i.e. below the 1 cpr frequency. In this case, the GGT trace (blue) is similar to V1 (red). So we see again a degradation with respect to the best case mainly at the 1 cpr peak.
- It can be concluded that in V1, V2 and V3 the cross-over frequencies (or at least one cross-over frequency for V1) are assumed too low. This indicates that the noise of the EGG is larger than the noise of the STR at the 1 cpr peak.
- For V4, the cross-over frequency for all components is at 5.7×10^{-4} Hz, which corresponds approximately to 3 cpr. In this case, the GGT trace (green curve) is clearly larger than the one for the best case (V3, cyan curve), mainly for frequencies from 3×10^{-4} Hz to about 1.5×10^{-3} Hz. In this frequency range, the GGT trace noise (green) is comparable with the trace from the nominal gradients (black). To a lesser extent also the frequencies around the first peak are degraded in this case. Thus, one can conclude that in V4 the cross-over frequencies have been chosen too high.

In summary, the test with different versions of stochastic models has shown that the GGT trace performance is best, when the cross-over frequency for all angular rate components is in the low between the first and second peak of the noise PSD. This corresponds to V3 of the assumed noise and weights for the Wiener filter. Therefore, in the next section all results of the Wiener method are based on V3. More generally, one can conclude from these tests that the EGG noise is smaller than the STR noise down to very low frequencies. Only for the frequencies corresponding to the 1 cpr peak and below the STR are performing better than the EGG, at the level of angular rates.

5 Results

In this section, the results of the new method for ARR, as well as the results of the STR combination and the new method for the computation of the IAQ are discussed. First, the influence at GG level is in the focus. Second, the impact on a gravity field solution is demonstrated.

5.1 Gravity gradients

To highlight the impact of the Wiener method for ARR, as well as the impact of the STR combination, four different sets of GG have been computed. They are summarized in Table 2. Besides the Wiener method for ARR, also the nominal algorithm for the ARR has been implemented. Therefore, it is not only possible to investigate the impact of the Wiener method with respect to the nominal method without STR combination (C vs. A) and the impact of the STR combination on the Wiener method (D vs. C), but also to study separately the impact of the STR combination on the nominal method (B vs. A). The performance of the four sets of GG can be evaluated using again the traceless condition of the GGT. Figures 9 and 10 show for two different days the PSD of the GGT trace of the four sets of GG. Figure 9 is an example of a day (Nov. 11th) where STR 2 is used in the nominal processing. Figure 10, in contrast, is an example of a day (Nov. 25th) where STR 1 is used in the nominal processing. This means that for the GG, which have been computed without STR combination (A and C), in Fig. 9 STR 2 was used, and in Fig. 10 STR 1.

Table 2 Four sets of GG

Name of GG set	Method for angular rate determination	STR combination
A	Nominal	No
B	Nominal	Yes
C	Wiener	No
D	Wiener	Yes

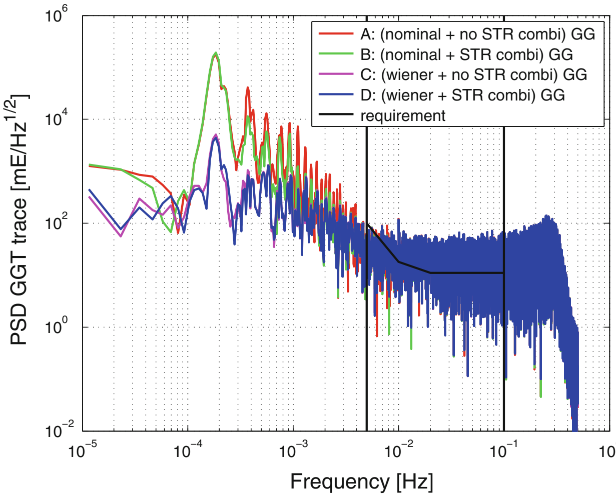

Fig. 9 GGT trace improvement; STR 2 in nominal processing; data from 11 November 2009

It can be noted:

- On both days, GG set A (nominal method, without STR combination (red)) has the largest noise PSD for the harmonics of the 1 cpr frequency.

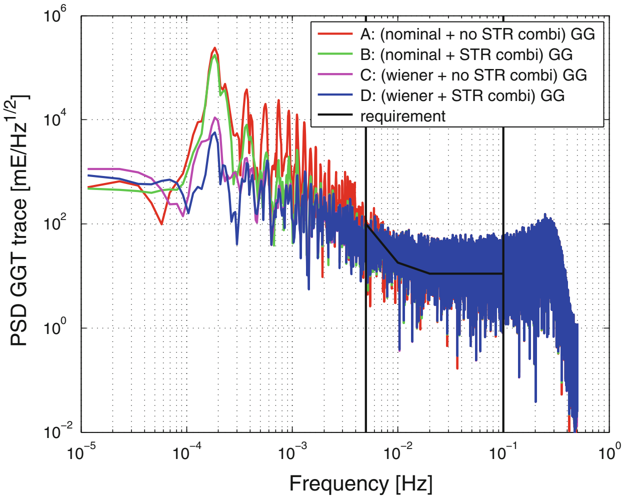

Fig. 10 GGT trace improvement; STR 1 in nominal processing; data from 25 November 2009

- In GG set B (nominal method, combined STR (green)) these peaks become smaller, except for the first peak (corresponding to 1 cpr), which is not significantly reduced.
- The improvement within the nominal method due to STR combination (set B with respect to set A) is larger when STR 1 (Fig. 10), and not STR 2 (Fig. 9) is used in the nominal processing.
- The GG sets C (magenta) and D (blue) show a significant improvement with respect to the sets A (red) and B (green). This indicates that the Wiener method performs significantly better than the nominal method. The improvement is largest at the 1 cpr peak.
- There is almost no difference between the GG sets C and D. This means that the STR combination has a much smaller effect than the use of the Wiener method. Only for those days where the nominal processing is based on STR 1 (Fig. 10), the first 1 cpr peak can be further decreased to some small extent.

In summary, four sets of GG have been spectrally analyzed by means of the GGT traceless condition. The GG from the nominal ARR without STR combination perform worst, whereas the GG from the Wiener method plus combined STR perform best below the MBW. Within the MBW there is (almost) no difference in the performance of all four cases. The improvement from STR combination alone is rather small.

5.2 Satellite-gravity-gradiometry gravity field solution

To evaluate the impact of the newly proposed method for ARR on the level of gravity field models, four scenarios have been tested. The fast gravity field processor quick look-gravity field analysis (QL-GFA) has been applied, which is also used in the frame of GOCE HPF in the regular processing chain, with short latency, for the purpose of system performance analysis. A detailed description of the architecture and functionality of the QL-GFA processor can be found in Pail et al. (2007). First operational results as provided in Mayrhofer et al. (2010) demonstrate that gravity field models with a quality competitive to rigorous gravity field solutions can be achieved by QL-GFA. The four configurations are in accordance with the scenarios A, C and D as discussed in Sect. 5.1, and are summarized in Table 3. The minuscules a and b indicate whether the nominal IAQ product or the improved quaternions as derived in Sect. 4.2 have been used. To analyze the sole effect of the new method, gravity field models based only on the satellite gravity gradiometry (SGG) components V_{XX}, V_{YY} and V_{ZZ} have been computed, and the SST component is disregarded. Since gravity field models derived from GPS orbits are also sensitive to the low to medium frequency range of the harmonic spectrum, they would partly mask the effect of the modifications discussed here. All gravity field computations are based on 26 days of input data from November 2009, and are resolved up to degree/order 200.

Spherical Cap regularization (Metzler and Pail 2005) has been applied as only constraint to the solution. The main feature of this regularization method is that it acts in space domain only at the polar gap areas (related to GOCE satellite's inclination of 96.5°), and leaves those areas covered by GOCE measurements unconstrained. Thus the results presented here are data-driven, but not significantly influenced by additional constraints.

One specific feature of the iterative QL-GFA method is the fact that after each iteration the residuals of the adjustment are analyzed and used as spectral weighting factors in the subsequent iteration (Pail et al. 2007). In this way, the error behavior is used to set up the observation error covariances (and correspondingly the metric of the normal equations), and thus is also reflected in the statistical coefficient error estimates.

Figure 11 shows the deviation of the estimated coefficients from the reference model ITG-Grace2010s (Mayer-Gürr et al. 2010) in terms of degree medians up to degree/order 180. Since the performance of GRACE is superior to GOCE in the

Table 3 Four scenarios for QL-GFA

Name of scenario	Method for angular rate determination	STR combination	IAQ
Aa	Nominal	No	Nominal
Ab	Nominal	No	New
Cb	Wiener	No	New
Db	Wiener	Yes	New

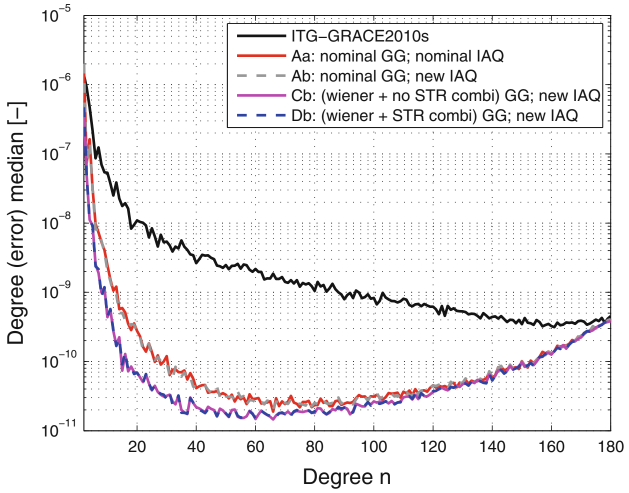

Fig. 11 Degree median differences between different scenarios and ITG-Grace2010s

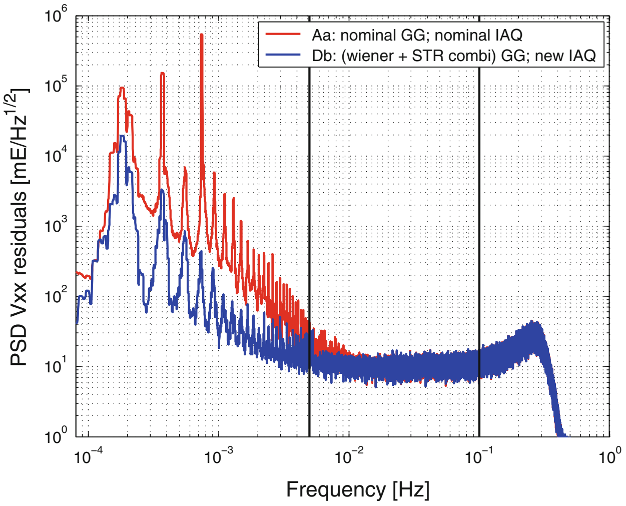

Fig. 12 PDS of residuals of gravity gradient component V_{XX}

low and medium degrees, it can serve as a reference solution to evaluate mainly the errors in the GOCE solutions.

Compared to the nominal scenario Aa (red curve), the results based on the newly derived gradient products applying the Wiener filter method (scenario Cb: magenta; scenario Db: blue) show a substantially improved performance mainly in the lower harmonic degrees up to degree/order 120, and even beyond for selected groups of coefficients, as it will be shown later. Scenario Ab with the nominal method for computation of the GG, but using the new IAQ (grey, dashed curve), does not give a significant improvement compared to the nominal configuration Aa (red curve). Also the difference of using combined (Db) or non-combined (Cb) STR data within the new method for ARR is negligible (compare blue and magenta curves).

Correspondingly, Fig. 12 shows the PSD estimates of the GG residuals after the gravity field adjustment, i.e. the difference between adjusted and original observations, exemplarily for the V_{XX} component. The residuals reflect the total errors in the system, projected onto the three main diagonal components of the GGT V_{XX}, V_{YY}, and V_{ZZ}. The red curve is related to the nominal scenario Aa (cf. also red curve in Fig. 11), while the blue curve displays the best scenario Db (corresponding to the blue curve in Fig. 11). Evidently, there are significant improvements mainly due to the new ARR method (and only very little due to STR combination), expressed by two main features (1) a generally improved performance below and in the lower MBW, and (2) a significant reduction of the peaks which occur as multiples of the 1 cpr frequency. These PSD estimates, which are, due to the gravity field adjustment, available for all individual gradiometer components, are in very good agreement with the results of the analysis of the GG trace (cf. Figs. 9, 10).

While the degree median plot in Fig. 11 gives an overall picture on the improvement in the harmonic spectrum, the details of the impact of the new ARR method can be seen even more lucidly when analyzing individual coefficients. Figure 13 shows the relative improvement of individual coefficients, computed from the error estimates (main diagonal elements of the a posteriori variance-covariance matrix) of the scenarios Aa and Db. Displayed is the ratio of standard deviations of the two solutions σ_{Aa}/σ_{Db}. As an example, a value of 2 means, that a certain coefficient could be improved by a factor of 2 due to the new ARR method. Two effects are evident: first, the accuracies of the low degree coefficients could be generally improved; this conclusion is in accordance with Fig. 11. In particular, the (near-)sectorial coefficients could be improved, because their accurate estimation requires relatively more information from below the MBW. Second, and equally important, the improvement occurs predominantly at characteristic bands at the orders $k \times 16$, with integer k, reflecting the mapping of the peaks of the gradiometer error spectra (cf. Fig. 12) onto the gravity field solution. These coefficients of order $k \times 16$ are particularly sensitive to those frequencies which show significantly degraded accuracies due to a lower signal to noise ratio. With the new ARR method, these stripes at orders $k \times 16$ are markedly reduced, i.e. the achievable accuracy for these coefficients is significantly increased. Since the largest differences (improvements) occur for these specific coefficients, the degree medians shown in Fig. 11 even underestimate the impact of the new ARR method. As Fig. 13 demonstrates, for selected groups of coefficients there is an impact up to high harmonic degrees. It shall be emphasized, that Fig. 13 shows a ratio of formal errors. However, due to the iterative weight adaptation used in QL-GFA as described above, it turns out to be a trustworthy estimate for the true errors. A similar plot

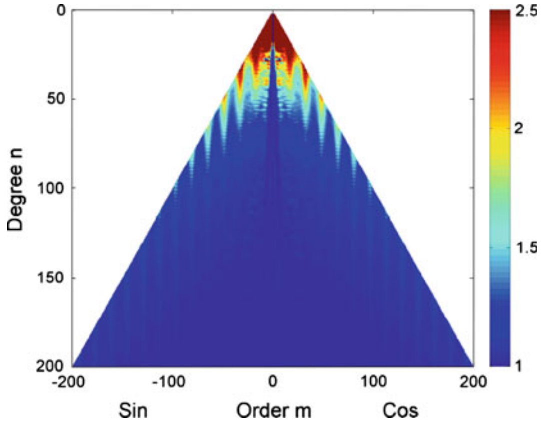

Fig. 13 Relative improvement in coefficients from solution Aa to Db due to new ARR method

of coefficient differences (not shown) of the two solutions Aa and Db reveal consistently the characteristic features of Fig. 13.

6 Conclusions

The complete processing chain from raw instrument data to gravity field solutions has been reproduced. Therefore, a comprehensive analysis and assessment of the impact of the new ARR method is possible. It is based on the optimal combination of STR and EGG data applying a Wiener filter. It is found, that for medium frequencies the STR noise is larger than it was expected from pre-launch simulations. The new ARR method takes into account the actual instrument noise characteristics and can deliver significantly improved GG below the MBW (and at the lower end of the MBW). This is verified by comparing the GGT trace of four sets of GG. Moreover, it is demonstrated that the use of combined STR data is useful, but has only a small effect on the achieved GG accuracy. At the gravity field level, improvements of selected groups of coefficients up to high harmonic degrees are observable when using the new ARR method. It is clear that the inclusion of the SST component (gravity from GPS orbit information) in the frame of a combined GOCE solution would to a large extent mask these improvements, because they occur mainly in the low to medium degree range of the harmonic spectrum. However, it is still worthwhile to extract as much information as possible from the new observation type of GOCE GG, also in the light of a combined SST and SGG solution, where gradiometry will get a higher relative weighting in the combination process. This is underlined by the fact, that for selected coefficient groups improvements are visible up to very high degrees. The analysis and quantification of the impact of the new ARR method for combined SST and SGG gravity field solutions, but also combinations with GRACE, will be the topic of further studies.

Acknowledgments We kindly acknowledge the provision of GOCE data via the EOLI-SA portal by ESA. The authors thank Reiner Rummel for his helpful discussions and comments on this work.

References

Best R (1991) Digitale Messwertverarbeitung. Oldenbourg, München

Bruinsma S, Marty J, Balmino G, Biancale R, Foerste C, Abrikosov O, Neumayer H (2010) GOCE Gravity Field Recovery by Means of the Direct Numerical Method. Proceedings of the ESA Living Planet Symposium, 28 June–2 July 2010, Bergen, Norway, ESA SP-686 (CD-ROM)

Cesare C, Catastini G (2008) Gradiometer On-Orbit Calibration Procedure Analysis. Technical Note to ESA, GO-TN-AI-0069, Issue 4, Alenia Aerospazio

Cesare C, Sechi G, Catastini G (2008) Gradiometer Ground Processing Algorithms Documentation. Technical Note to ESA, GO-TN-AI-0067, Issue 7, Alenia Aerospazio

Drinkwater M, Haagmans R, Muzzi D, Popescu A, Floberghagen R, Kern M, Fehringer M (2007) The GOCE gravity mission: ESA's first core explorer. In: Proceedings 3rd GOCE user workshop, European Space Agency, Noordwijk, ESA SP-627, pp 1–8

Frommknecht B (2008) Integrated Sensor Analysis of the GRACE Mission. DGK, Reihe C, 617, Verlag der Bayerischen Akademie der Wissenschaften, München

Frommknecht B, Stummer C, Gilles P, Floberghagen R, Cesare S, Catastini G, Meloni M, Bigazzi A (2010) GOCE L1b Processing. Proceedings of the ESA Living Planet Symposium, 28 June–2 July 2010, Bergen, Norway, ESA SP-686 (CD-ROM)

Gruber T, Abrikosov O, Hugentobler U (2010a) GOCE High Level Processing Facility; GOCE Standards. Tech. Rep. GO-MA-HPF-GS-0111, Issue 3.2

Gruber T, Rummel R, Abrikosov O, van Hees R (2010b) GOCE High Level Processing Facility; GOCE Level 2 Product Data Handbook. Tech. Rep. GO-MA-HPF-GS-0110, Issue 4.2

Johannessen J (1999) Gravity Field and Steady-State Ocean Circulation Mission. Tech. Rep. ESA SP-1233(1), Noordwijk

Jørgensen J (2003) ASC GOCE design and performance report. Technical Note to ESA, GO-RP-DTU-2018, Issue 1.1

Kern M, Haagmans R, Plank G, Lamarre D, Floberghagen R, Drinkwater M (2007) In-flight GOCE gradiometer calibration and validation. American Geophysical Union, Fall Meeting 2007, abstract G33A-0894

Lamarre D (2008) Algorithm description: retrieval of gradiometer parameters. Version 2.0 draft, 23 April 2008

Mayer-Gürr T, Eicker A, Kurtenbach E, Ilk K (2010) ITG-GRACE: Global static and temporal gravity field models from GRACE data. In: Flechtner F, Mandea M, Gruber T, Rothacher M, Wickert J, Güntner A, Schöne T (eds) System Earth via Geodetic-Geophysical Space Techniques, Advanced Technologies in Earth Sciences, pp 159–168. doi:10.1007/978-3-642-10228-8_13, ISBN: 978-3-642-10227-1

Mayrhofer R, Pail R, Fecher T (2010) Quick-look gravity field solution as part of the GOCE quality assessment. Proceedings of the ESA Living Planet Symposium, 28 June–2 July 2010, Bergen, Norway, ESA SP-686 (CD-ROM)

Metzler B, Pail R (2005) GOCE data processing the spherical cap regularization approach. Stud Geophys Geod 49: 441–462. doi:10.1007/s11200-005-0021-5

Migliaccio F, Reguzzoni M, Sansó F, Tscherning C, Veicherts M (2010) GOCE data analysis: the space-wise approach and the first space-wise gravity field model. Proceedings of the ESA Living Planet Symposium, 28 June–2 July 2010, Bergen, Norway, ESA SP-686 (CD-ROM)

Pail R (2005) A parametric study on the impact of satellite attitude errors on GOCE gravity field recovery. J Geod 79: 231–241. doi:10.1007/s00190-005-0464-z

Pail R, Metzler B, Preimesberger T, Lackner B, Wermuth M (2007) GOCE quick look—gravity field analysis in the framework of HPF. In: Proceedings 3rd GOCE user workshop, European Space Agency, Noordwijk, ESA SP-627, pp 325–332

Pail R, Goiginger H, Mayrhofer R, Schuh W, Brockmann J, Krasbutter I, Höck E, Fecher T (2010) Global gravity field model derived from orbit and gradiometry data applying the time-wise method. Proceedings of the ESA Living Planet Symposium, 28 June–2 July 2010, Bergen, Norway, ESA SP-686 (CD-ROM)

Papoulis A (1984) Signal analysis. McGraw-Hill, New York

Rispens S, Bouman J (2009) Calibrating the GOCE accelerations with star sensor data and a global gravity field model. J Geod 83: 737–749. doi:10.1007/s00190-008-0290-1

Rummel R (1986) Satellite Gradiometry. Lecture Notes in Earth Sciences 7:317–363, Springer, Berlin

Rummel R, Gruber T, Koop R (2004) High Level Processing Facility for GOCE: Products and Processing Strategy. In: Lacoste H (ed). Proceedings of the 2nd International GOCE User Workshop “GOCE, The Geoid and Oceanography”, ESA SP-569

Stummer C, Rispens S (2009) How to get gravity gradients from the GOCE measurements. Paper presented at the IAG 2009 Scientific Assembly “Geodesy for Planet Earth”, 31 August–4 September 2009, Buenos Aires, Argentina

Visser P (2008) Exploring the possibilities for star-tracker assisted calibration of the six individual GOCE accelerometers. J Geod 82: 591–600. doi:10.1007/s00190-007-0205-6

Wittenburg J (1977) Dynamics of systems of rigid bodies. BG Teubner, Stuttgart